Porous Metallophilic Frameworks Incorporating Metal-Organic Chains as Humidity Sensors Exploring Uranyl Photoluminescence

Jakub J. Zakrzewski, Damian Jędrzejowski, Junhao Wang, Hiroko Tokoro, Shin-ichi Ohkoshi, Dariusz Matoga, Szymon Chorazy**

Jakub J. Zakrzewski, Damian Jędrzejowski, Dariusz Matoga, Szymon Chorazy
Faculty of Chemistry, Jagiellonian University, Gronostajowa 2, 30-387 Kraków, Poland
E-mail: j.zakrzewski@uj.edu.pl; simon.chorazy@uj.edu.pl

Jakub J. Zakrzewski, Damian Jędrzejowski
Doctoral School of Exact and Natural Sciences, Jagiellonian University
Łojasiewicza 11, 30-348 Kraków, Poland
E-mail: j.zakrzewski@uj.edu.pl

Junhao Wang, Hiroko Tokoro
Department of Materials Science, Institute of Pure and Applied Sciences, University of Tsukuba, 1-1-1 Tennodai, Tsukuba, Ibaraki 305-8573, Japan

Shin-ichi Ohkoshi
Department of Chemistry, School of Science, The University of Tokyo, 7-3-1 Hongo, Bunkyo-ku, Tokyo 113-0033, Japan

Keywords: luminescent materials, optical sensors, humidity sensing, metal-organic frameworks, metallophilic interactions, uranyl, cyanides

Abstract

Luminescent coordination polymers, including metal-organic frameworks, serve as a platform for optical sensing of physical and chemical stimuli, including temperature or pressure for the former, or gases, solvent vapors, explosives, toxic species, etc. for the latter. The related materials built of uranyl cations, UO_2^{2+}, remain unexplored, despite their tunable photoluminescence. While recently, bimetallic coordination and supramolecular systems built of cyanido metal complexes were proven a successful pathway towards stimuli-responsive materials, their combination with uranyl species is limited. Here, we report the construction of novel uranyl-based systems demonstrating a distinct sensitivity of emission to solvent vapors, which was achieved by generating metal-organic, i.e, uranyl–2,4'-bipyridine-N,N'-dioxide, chains that are arranged into a porous supramolecular framework by metallophilic interactions between attached tetracyanidometallates(II), $[M^{II}(CN)_4]^{2-}$ (M^{II} = Pd, **1**; Pt, **2**). Both resulting materials reveal reversible single-crystal-to-single-crystal transformation upon removal of crystallization solvent molecules, which is due to the flexibility of metallophilic interactions forming a porous metallophilic framework resembling MOF-74. The presence of infinite channels introduces sensing capabilities to water vapors while the emissive character leads to the humidity-variable emission characteristics, including the strong variation in emission intensity and lifetime. The obtained systems exhibit repeatable adsorption and emission characteristics, meeting the criteria for luminescent sensors.

1. Introduction

Luminescent coordination systems, such as coordination polymers (CPs) and metal-organic frameworks (MOFs), or even luminescent supramolecular frameworks based on metal complexes, gather enormous scientific interest due to their applications in different branches of technology and modern life.[1] For several decades, luminescent species have been employed in the construction of light emitting devices,[2] anti-counterfeiting inks,[3] optical thermometers or pressure sensors,[4] and developed to construct materials for energy storage and conversion,[5] diagnostics,[6] as well as sensors of volatile gases and solvents, energetic compounds, drugs, and toxins, etc.[7] In this regard, the coordination chemistry approach introduces a rational design of desired optical properties throughout the selection of metal ions and ligands, used either to harvest and transfer the energy or to emit light itself through ligand-centered (LC) or charge-transfer (CT) electronic transitions.[8] The construction of CPs and supramolecular frameworks often introduces other physical functionalities, leading to multifunctional materials, which may result in coupling between luminescence and the group of magnetic, dielectric, and

mechanical phenomena.[9] Among such, MOF materials were demonstrated to the broadest extent as a perfect platform to observe the interplay between optical properties and porosity.[10] Recently, their analogs exploring supramolecular interactions instead of coordination bonds, i.e., porous supramolecular frameworks (often named supramolecular assembly frameworks, SAFs), also draw attention due to their porosity combined with other physical properties.[11] Within a library of such porous materials taking advantage of coordination chemistry, many physical phenomena were reported.[12] They were recognized by designable pore size and sorption properties,[13] catalytic,[14] luminescent,[15] and electrical effects,[16] as well as applications in drug delivery,[17] gas separation,[18] and hydrogen storage.[19] Their rational design and crystallinity allow structure-property correlations,[20] which enables optimization of their properties. The design of luminescent MOFs (L-MOFs) employs rather well-recognized rules for both metal nodes and linkers.[1cd,7a,15] For the former, the most recognized are d^{10} metal centers, e.g., Zn^{2+} or Cd^{2+}, or alkaline earth metals, e.g., Mg^{2+}, as their use facilitates the observation of LC emission.[21] On the other hand, the d^8 configuration of Ag^{I}, Au^{I}, Pt^{II}, and Pd^{II} centers serves as a prerequisite for the metal-to-ligand CT emission.[22] Frequently, to construct L-MOFs, the presence of 4f-block metal ions is introduced.[23] However, due to low absorption coefficients for f-f transitions, the presence of the antennae effect remains crucial for generating a strong emission signal.[24] Both d- and 4f-block metal-based L-MOFs were utilized to construct materials, where luminescence was accompanied by porosity.[8b,25] Such conjunction resulted in the sensing of chemical factors, including amine vapors,[26] solvents,[27] metal ions,[28] anions,[29] nitroaromatics,[30] and biochemical analytes,[31] using an emission read-out. Recently, the analogous results were found accessible for SAFs, where emissive metal complexes, clusters, or organic species were arranged in porous supramolecular frameworks.[32] While the construction of luminescent Ln(III) complexes and MOFs is one of the hottest topics within coordination chemistry, the related attention devoted to actinides is rather small.[33] Their intrinsic electronic properties, such as relativistic effects, are suspected to result in unique magnetic and optical properties.[34] Moreover, the construction of actinide-based materials is considered an attractive method for the recycling of radionuclide wastes, originating from the development of nuclear weapon programs and energy production. In these aspects, the synthesis of novel materials, especially those based on rather stable ^{232}Th and ^{238}U isotopes, can be considered an alternative to the design of customized ligands for complexing d- and 4f-block metal centers.[35] Actinide complexes may be emissive, showing even circularly polarized luminescence,[36] while actinide-based porous systems, mainly MOFs (An-MOFs), were shown to build a variety of topologies due to their structural flexibility. The most recognized ion within

An-MOFs is the uranyl(VI) cation, $U^{VI}O_2^{2+}$, known for its visible light emission of the LMCT origin,[37] which was used for photocatalysis and photoelectric conversion.[38] On the other hand, complexes of U-centers of lower valency were studied due to catalytic activity and magnetism.[39] Nevertheless, the stability of the (+6) oxidation state and rigid linear geometry of the uranyl(VI) cation enables a rational design of coordination systems exhibiting, e.g., selective affinity to various organic molecules.[40] Moreover, such materials may reveal some degree of flexibility as observed by a single-crystal-to-single-crystal (SC-SC) transformation found upon the exposition toward solvents.[41] Despite the rich chemistry of uranyl(VI) cations, to the best of our knowledge, their emission was never tested for sensing humidity.[42]

Among coordination compounds based on actinide ions, only a few of them were constructed using cyanido metal complexes (CMCs) serving as counter-ions or metalloligands.[43] In contrast, for d- and 4f-block metal-based coordination systems, CMCs were proven fruitful for the generation of desired magnetic, optical, dielectric, and mechanical phenomena,[44] and combining them in multifunctional materials.[45] For several d-block metal ions, CMCs exhibit luminescence of different origins,[46] including metal-centered and LMCT emission, and even metal-to-metal-to-ligand charge transfer (MMLCT) emission attributed to metallophilic interactions between di- and tetracyanidometallates of Ag^I/Au^I and Pd^{II}/Pt^{II}, respectively.[47] CMC-based CPs often reveal great responsivity to physical stimuli, including temperature or pressure,[48] and light.[49] Considering the influence of chemical stimuli, the most recognized CMC-based coordination compounds belong to the family of Hofmann-type networks based on tetracyanidometallates, showing the spin crossover effect affected by guest molecules.[50,51] The vast majority of CMC-based coordination compounds crystallize with solvent molecules. Then, their post-synthetic desolvation often leads to modified optical and magnetic properties.[52] Moreover, the influence of humidity on the set of physical properties of CMC-based materials was reported,[45b,48a,53] including fine-tuning of Ln(III)-centered emission.[54] However, within a small library of CPs composed of actinides and CMCs, only a few examples showed emission, while the impact of external stimuli upon their properties remained unexplored.[43b,55]

Here, we report the synthesis and systematic studies of novel emissive porous materials built of uranyl(VI) cations and tetracyanidometallates. We used an organic linker, 2,4'-bipyridine-N,N'-dioxide (2,4'-bpdo) together with bridging $[M^{II}(CN)_4]^{2-}$ (M^{II} = Pd (**1**), Pt (**2**)) ions which result in the self-assembly of infinite metal-organic chains expanding along the *c* axis. They are further combined by M^{II}–M^{II} metallophilic interactions producing one-dimensional pores filled by crystallization water molecules, thus the remarkable type of porous supramolecular frameworks, i.e., porous metallophilic frameworks, are here reported. Upon exposition towards

the elevated temperature and/or in an inert gas flow, the crystallization solvent molecules are reversibly removed within an SC-SC transformation. The two reported porous metallophilic frameworks, $\{[U^{VI}O_2(2,4'\text{-bpdo})(H_2O)][M^{II}(CN)_4]\}\cdot nH_2O$ (M^{II} = Pd (**1**), Pt (**2**); n = 0–4) are sensitive to water vapors (humidity), as confirmed by a thorough analysis of water adsorption properties. Their green photoluminescence was employed to study the change in the water content within the porous structure, and the impact of variable humidity was found to affect distinctly and repeatedly both the emission intensity and the emission lifetime.

2. Results and discussion

Yellow needle single crystals of **1**, suitable for the X-ray diffraction experiment, were obtained by the slow evaporation of a water solution containing uranyl(VI) nitrate, $U^{VI}O_2(NO_3)_2\cdot 5H_2O$, 2,4'-bipyridine-N,N'-dioxide (2,4'-bpdo), and $K_2[Pd^{II}(CN)_4]\cdot nH_2O$. The use of $K_2[Pt^{II}(CN)_4]\cdot nH_2O$, instead, gave similar crystals of **2**, being suitable for the single-crystal X-ray (SC-XRD) diffraction studies (see Experimental details in Supporting Information, **Figure** 1 and S1–S3, and **Table** S1–S6).[56] For both materials, the composition of crystals was established by the SC-XRD method, showing the analogous, general formula of $\{U^{VI}O_2(2,4'\text{-bpdo})(H_2O)][M^{II}(CN)_4]\}\cdot 4H_2O$ (M^{II} = Pd (**1**), Pt (**2**)).[57] For the as-synthesized phases, the crystal structure is comprised of hybrid chains of the I^1O^1 connectivity, where every uranium(VI) center coordinates one aqua ligand, two oxido ligands, two bridging 2,4'-bpdo ligands, and two bridging $[M^{II}(CN)_4]^{2-}$ moieties (**Figure** 1). Within the coordination chain structure, to connect two uranium(VI) centers through both organic and inorganic linkers, two $\{U^{VI}\text{-}(2,4'\text{-bdpo})\text{-}U^{VI}\}$ and three $\{U^{VI}\text{-}[M^{II}(CN)_4]^{2-}\text{-}U^{VI}\}$ linkages should be considered, which is due to corrugated nature of the inorganic chain based on *cis*-binding $[M^{II}(CN)_4]^{2-}$ units. Despite this, only one U(VI) center is symmetry independent and adopts the geometry of a distorted pentagonal bipyramid, as determined by a Continuous Shape Measure (CShM) analysis, with its two oxido ligands of the uranyl(2+) cation, two oxygen atoms of the 2,4'-bpdo ligands, two nitrogen atoms of the N-bonded cyanido ligands, and one O-atom of an aqua ligand.[58]

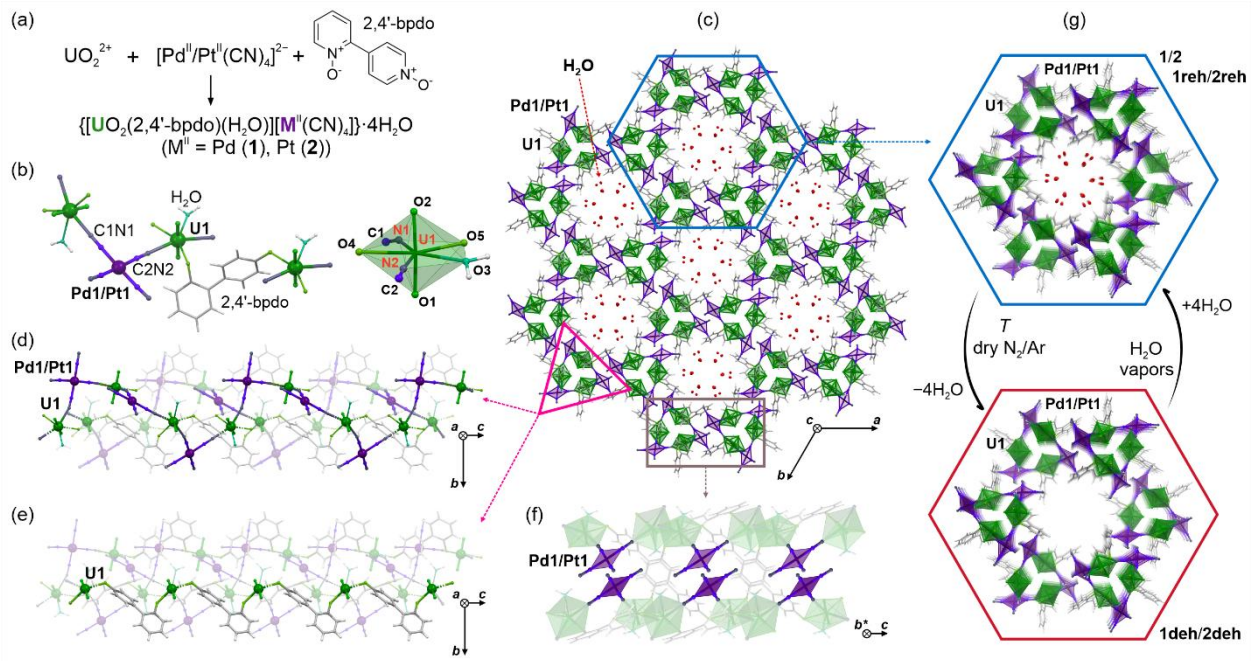

Figure 1. The synthesis of **1** and **2** (a) as well as the crystal structure of **1** and **2**, their dehydrated (**1deh**, **2deh**, respectively), and their rehydrated phases (**1reh**, **2reh**, respectively) (b–g), including the molecular unit of the $\{U^{VI}M^{II}\}_n$ (M^{II} = Pd, Pt) chains of **1** and **2**, shown with the geometry of the U^{VI} first coordination sphere (b), the structural view of the supramolecular arrangement of chains of **1** and **2** along the *c* crystallographic axis (c), the structure of the related $\{U^{VI}M^{II}\}$ chain with the highlighted cyanido-bridged connectivity (d), the structure of the related $\{U^{VI}M^{II}\}$ chain with the highlighted organic ligand (2,4'-bpdo) connectivity (e), the visualization of the metallophilic interactions between $[M^{II}(CN)_4]^{2-}$ complexes of related neighboring chains (f), the close-up of the infinite channels positioned along the *c* axis in **1**, **2**, **1reh**, and **2reh**, which are occupied by water molecules of crystallization, together with the analogous empty channels found within the single-crystal structures of the dehydrated phases, **1deh** and **2deh** (g). Note that the structural models obtained for **2** and **2deh** were used to visualize the structural features of **1**/**2**/**1reh**/**2reh** and **1deh**/**2deh**, respectively (see Supporting Information for detailed views of all these crystalline phases).

The obtained metal-organic chains form helical structures expanding parallel to the *c* axis of the $R\bar{3}$ space group; however, the presence of both Δ and Λ helices results in the presence of the inversion center. The neighboring chains of different chirality interact with each other *via* hydrogen bonds between both H-atoms of the aqua ligand coordinated by the U(VI) center and terminal cyanido ligands of $[M^{II}(CN)_4]^{2-}$ units, More importantly, the alignment of metal-organic chains within the material is governed by metallophilic interactions between the d^8 metal centers of a square planar geometry (**Figure** 1f, **Table** S5). The resulting arrangement of

chains within the supramolecular network, which can be named a metallophilic framework, forms a honeycomb topology similar to the well-known MOF-74 system (**Figure** 1).[59] As a result, along the *c* axis, infinite channels, occupied by the water molecules of crystallization, are located. Then, by eliminating water molecules in the interstitial space, the volume of channels is calculated as 23.1% and 23.4% of the unit cell volume for **1** and **2**, respectively (probe radius of 1.2 Å),[60] suggesting the porous nature of obtained metallophilic frameworks. Water molecules of crystallization found for **1** and **2** lack the exact assignment of hydrogen atoms, despite collecting high-quality X-ray diffraction data (**Table** S1 and S2). Moreover, short contacts involving the located O-atoms indicate the presence of a weak hydrogen bonding motif involving the non-coordinated solvent.

As suggested by the TG analysis, the air-dried samples of **1** and **2** readily lose water molecules even at room temperature in the presence of dry N_2 flow (**Figure** S4). Following these findings, single crystals of **1** and **2**, mounted on the goniometer, were heated *in situ* up to 320 K in the flow of N_2 and kept for an hour to complete the transformation to the dehydrated phases of **1deh** and **2deh**, respectively (**Figure** 1g). After cooling the crystals, fine diffraction images were observed suggesting the single-crystal-to-single-crystal (SC-SC) nature of the dehydration process. Therefore, the SC-XRD analysis was repeated for the crystals of the dehydrated phases after cooling the crystals to 100(2) K. The obtained data revealed that after the dehydration only subtle changes within the coordination skeleton of **1deh** and **2deh** are observed (**Figure** S1–S3, **Table** S1–S6). The first coordination sphere for U(VI) centers in **1deh** and **2deh** keep the only coordinated aqua ligand, and the overall change of the unit cell volume reaches only ca. 2.6% and 2.4%, respectively. As a consequence, the infinite channels along the *c* axis are retained after the dehydration of **1** and **2**, with their final volumes being at the level of 21% of the unit cell volumes. Only subtle changes can be also found within the remaining short contacts (**Table** S6), while the closest $M^{II}…M^{II}$ distances may be considered unaffected (**Table** S3). These values support the statement about the rigidity of the supramolecular network attributed to the combined effects of H-bonding contacts between the coordinated aqua ligand and terminal cyanido ligands, and metallophilic interactions between $[M^{II}(CN)_4]^{2-}$ units. However, noticeable geometrical changes related to the overlap between the $[M^{II}(CN)_4]^{2-}$ moieties involved in the formation of metallophilic interactions appear, suggesting a sponge-like behavior, leading to the relative stability of the whole material regardless of the exact water uptake into the channels between 0 and 4 molecules per formula unit. Such a feature also suggests possible rehydration of **1deh** and **2deh** crystals within a SC-SC manner, which was proven by placing the crystals for 24 h in a closed vial with a small amount of distilled

water at the bottom. The obtained **1reh** and **2reh** crystals show the increase of the unit cell volume related to the recovery of water molecules inside the channels, occupying the same crystallographic positions as found for **1** and **2** (**Figure** S1–S3, **Table** S1–S6). The obtained results of the SC-XRD analysis were confirmed also by the *T*-variable IR absorption spectroscopy and powder X-ray diffraction analysis. The collected IR spectra for **1** and **2** possess broad absorption bands above 3000 cm^{-1}, which are partially related to the number of the O–H stretching vibrations involving H-bonded water molecules of crystallization (**Figure** S5). After the thermal dehydration in the N_2 flow, the intensity of this part of the spectra decreases; however, the non-zero absorption still appears for both **1deh** and **2deh** phases, owing to the presence of aqua ligands in the U(VI) first coordination sphere. Different maxima related to the stretching vibrations of cyanido ligands in the 2250–2000 cm^{-1} remain almost unaffected during dehydration, as well as those positioned in the organic fingerprint part of the spectra.

On the other hand, the set of experimental and calculated powder X-ray diffraction patterns (P-XRD), supports the phase purity of the samples and validity of the SC-XRD analysis (**Figure** S6). The samples of **1deh** and **2deh** for the P-XRD experiments were obtained in a dry inert gas atmosphere without further heating. The latter suggests that **1** and **2** are sensitive just to changes in the value of the relative humidity at room temperature. The reversibility of the dehydration in a dry atmosphere was also analogously proven by the P-XRD method to the SC-XRD experiments (**Figure** S7). Moreover, the air-stable phases of **1** and **2** reveal P-XRD patterns almost unchanged to powder samples protected by the mother solution. However, both the CHN elemental analysis and the TGA (**Figure** S4) prove that the air-stable phases contain ca. 3 water molecules of crystallization per the $\{U^{VI}M^{II}\}$ unit, which gives $\{[U^{VI}O_2(2,4'\text{-bpdo})(H_2O)][Pd^{II}(CN)_4]\}\cdot 3H_2O$ and $\{[U^{VI}O_2(2,4'\text{-bpdo})(H_2O)][Pt^{II}(CN)_4]\}\cdot 3H_2O$ compositions for **1** and **2**, respectively.

Both reported materials were obtained as powder samples of a greenish-yellow color which is mainly attributed to the presence of uranyl(VI) moieties. Within the solid-state UV-vis absorption spectra collected for **1** and **2**, a broad band is present above ca. 380 nm, which overlaps with the strong UV absorption related mainly to the presence of the 2,4'-bpdo ligand (**Figure** S8).[43b] Nevertheless, within the visible-light absorption, a distinct set of peaks can be noticed, which is due to the vibronic coupling of uranyl(VI) CT electronic states to the fully symmetric $O\text{-}U^{VI}\text{-}O$ stretching vibration. Analysis of the UV-light absorption should involve two main contributions: (a) $n \rightarrow \pi^*/\pi \rightarrow \pi^*$ transitions of the 2,4'-bpdo, as mentioned above, and (b) MMLCT transitions originating from the presence of metallophilic M^{II}–M^{II} (M = Pd, Pt) interactions.[61] The impact of the MMLCT bands should be rather negligible, due to large

intermetallic distances both for **1** and **2** of ca. 3.6 Å, accompanied by the small overlap between complexes in the supramolecular lattice. Moreover, the position of the MMLCT band can span between UV and visible ranges in the form of a broad background, thus the observed structure for the electronic spectra should be mainly attributed to 2,4'-bpdo and UO_2^{2+} moieties, with an additional maximum for **2** located at ca. 280 nm, which corresponds to the absorption of the isolated $[Pt^{II}(CN)_4]^{2-}$ complexes.[62]

Owing to the structural dynamics regarding the non-coordinated solvent in **1** and **2**, for both systems room-temperature water adsorption properties were studied using gravimetric and volumetric methods (**Figure** 2 and S9–S13). Preliminary studies using the TG apparatus coupled with a humidity generator revealed considerable sample mass increase upon adsorption of water (**Figure** S9). Further, the detailed adsorption and desorption curves were collected using the Dynamic Vapor Sorption (DVS) method at 25°C. Each point was stabilized until the mass change, dm/dt, reached less than 0.002% min^{-1}. Initially, both samples were dehydrated at 0 RH to reach the stable mass; then, the full cycle of adsorption and desorption was collected at the stable temperature (**Figure** 2ac). According to the structural analysis, the mass of the sample at 0 RH corresponds to the dehydrated phase of **1** (**1deh**; or **2deh**) with the composition given by the formula $\{[U^{VI}O_2(2,4'\text{-bpdo})(H_2O)][M^{II}(CN)_4]\}$ (M^{II} = Pd (**1deh**), Pt (**2deh**)). Upon increasing water partial pressure, within the first step, only a small amount of water is adsorbed, suggesting a relatively weak affinity of the channels' interior towards polar molecules.

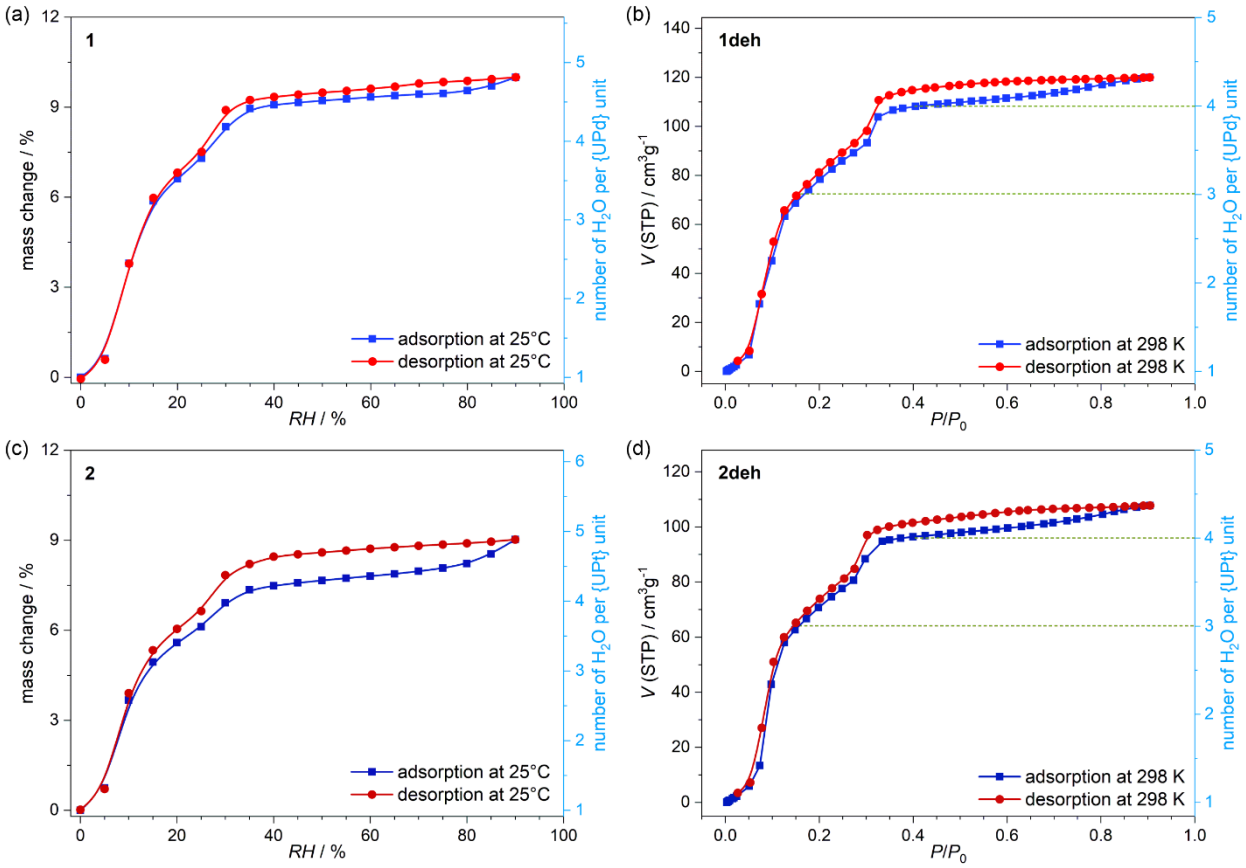

Figure 2. Water vapor sorption properties investigated by a gravimetric method using Dynamic Vapor Sorption (DVS) apparatus for **1** (a) and **2** (c), and by a volumetric technique for the thermally dehydrated (10^{-3} mbar, 50°C) samples, **1deh** (b) and **2deh** (d). In each case, the correlation of the gravimetric or volumetric curves with the number of water molecules per {UM} (M = Pd, Pt) unit is presented. Note that the related scales (light blue scales on the right side of each graph) start with 1 as it corresponds to a single coordinated water molecule (per formula unit) which is removed neither at 0 RH nor even using heating under vacuum.

However, at 10% RH, more than 1 water molecule inside the channels is already adsorbed, which is followed by adsorption of another water molecule per $\{U^{VI}M^{II}\}$ unit at 15% RH. Then, further adsorption occurs following a different trend with a smaller slope up to ca. 30% RH, where 3 water molecules accommodate channels of the porous structure (thus, the total number of 4 water molecules per formula unit is here reached). The last step in both adsorption and desorption curves is extremely gradual and corresponds to the sorption of one more additional water molecule per formula unit; however, up to ca. 90% RH, a transformation towards the fully hydrated phase (i.e., the phase corresponding to the crystal structure shown in **Figure** 1) seems to be incomplete. Upon decreasing relative partial pressure, a desorption course is different from the original one, i.e., the hysteretic behavior is observed, and the discrepancy

between adsorption and desorption curves is more visible for **2**. Such an effect may originate from the formation of a hydrogen bonding network between non-coordinated water molecules inside channels. Down to 15% RH for **1** and 10% RH for **2** the divergence between adsorption and desorption curves can be noticed. Such a behavior correlates well with the fact that for two adsorbed water molecules per formula unit the energy of breaking the H-bonding network should be minimalized.

Additional analysis of water adsorption properties is given by the sorption studies collected using a volumetric method (**Figure** 2bd). Firstly, the porosity assessment of **1deh** and **2deh** after degassing was substantiated through sorption analysis employing nitrogen and carbon dioxide as adsorbates (**Figure** S10). Experimental findings indicated the absence of porosity in both materials concerning these adsorbates, with a maximal sorption capacity attaining merely 5% of the anticipated pore volume as projected by the crystal structure. The maximal specific surface area determined through the Brunauer-Emmett-Teller (BET) method reached 30 m^2/g, aligning with physisorption occurring predominantly on the exterior surface of the material.[63] Next water vapor was selected owing to its inherent presence within **1** and **2** pores, as well as its elevated dipole moment and significant involvement in forming interactions with the materials' framework. The resulting isotherm profile reflected the microporous nature of the materials, characterized by step adsorption of discrete portions of the adsorbate (**Figure** 2 and S11–S13). The conclusions from the initial steps of adsorption are almost unchanged from the DVS method; however, at higher relative partial pressure a slightly decreased number of adsorbed water molecules is observed. Nevertheless, up to 0.9 P/P_0 (90% RH), the amount of adsorbed water remains at the level of ca. 3.5 molecules per formula unit (i.e., the total number of ca. 4.5 molecules per formula). Similar to the DVS measurements, the desorption and the adsorption curves differ at higher relative partial pressure and converge at the values corresponding to 2 water molecules per formula unit and less for both **1** and **2**. The detailed analysis of the volumetric adsorption/desorption curve at the variable temperatures indicates that the step related to the adsorption of the 3rd water molecule shows the highest dependence on temperature. At the decreased temperature of 283 K, the step of the 3rd water adsorption appears below 0.2 P/P_0 (20% RH) for **1** or even 0.15 P/P_0 (15% RH) for **2**, while increasing temperature by 20 K results in extremely gradual adsorption, starting at the same relative pressure value, but finishing above 0.4 P/P_0 (40% RH) for both materials.

The distinctive shape of the sorption curve, along with its *T*-dependent variation (**Figure** S11–S13), prompted a thorough exploration of the isosteric heat of adsorption (**Figure** 3).[64] Initial examination of this graph suggests a consistent heat of adsorption ranging between 49

and 51 kJ/mol for adsorption of the initial two water molecules in both materials. After the adsorption of these initial two molecules, a gradual increase of the heat of adsorption is observed culminating in values of 62.4 and 69.0 kJ/mol, for **1deh** and **2deh**, respectively.

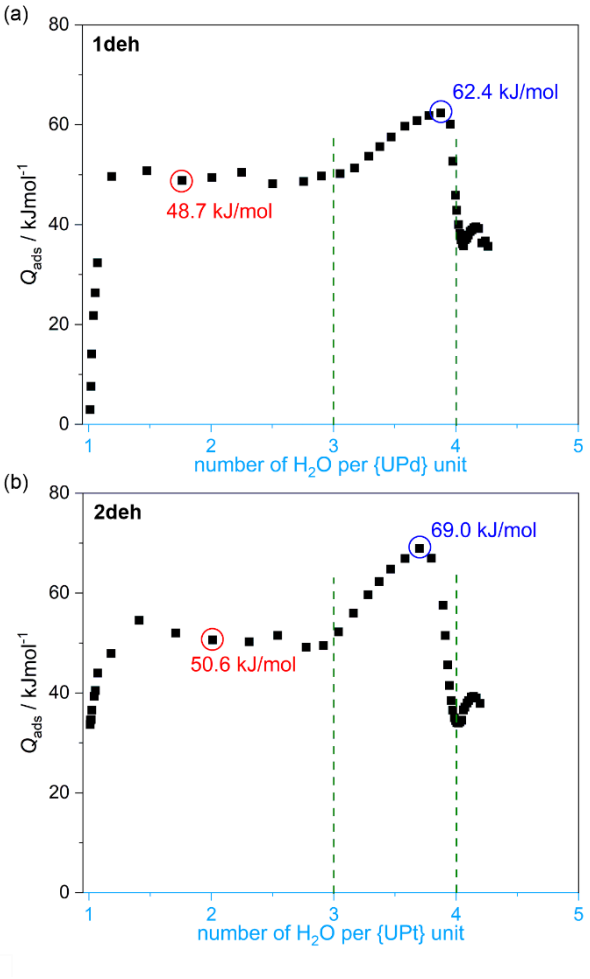

Figure 3. Isosteric heat of water adsorption plots as the functions of the number of adsorbed water molecules per formula unit for **1deh** (a) and **2deh** (b). The red circles with indicated values correspond to the isosteric heat for the two first adsorbed water molecules adsorbed while the dark blue circles with indicated values are related to the uptake of three water molecules. The vertical green dotted lines emphasize the range of the adsorbing of the third water molecule which corresponds to the distinct step observed on the respective volumetric curves (**Figure** 2bd). Please note that, similarly to the graphs in **Figure** 2, the scales corresponding to the number of water molecules per formula unit (light blue scales) start with 1 which is due to the presence of coordinated water molecules (1 per formula unit) that are not involved in the sorption-desorption processes (**Figure** 1).

This elevation corresponds to shifts in the position of the second step on the adsorption isotherms and is indicative of the augmented affinity of the material for the third adsorbed water molecule. Upon the adsorption of three water molecules, a precipitous decline in the heat of adsorption ensues, with the residual adsorbed quantity attributed to adsorption (condensation) on the surface of the crystallites, characterized by a heat of adsorption commensurate with the enthalpy of vaporization of water. The observed values of heat of adsorption imply a homogeneous environment for the first two adsorbed water molecules. The estimated enthalpy of four hydrogen bonds between water molecules approximates 40 kJ/mol, suggesting the predominant involvement of these water molecules in H-bonding among themselves, augmented by an additional stronger interaction elevating the heat of adsorption by approximately 25% relative to the enthalpy of hydrogen bonds in water. Conversely, the behavior for the third adsorbed water molecule diverges significantly, manifesting a substantially higher heat of adsorption, surpassing the enthalpy of hydrogen bonds in water by over 70% for the **2deh** material, indicative of additional robust interactions with the material's framework.

Both **1** and **2** under UV light excitation reveal pronounced green emission originating from the photoluminescence of UO_2^{2+} cations. The related photos of the emission were gathered both for air-stable and water-immersed powder samples (**Figure** 4). Within the room-temperature emission pattern, the set of six maxima can be distinguished for both **1** and **2**, which is typical of the vibronically-coupled character of the charge-transfer emission (**Figure** 5 and S14).[65] The most intense maxima are located at 515 nm and 516 nm for **1** and **2**, respectively, with additional strong bands being positioned on its two sides at ca. 494 and 539 nm for both systems. However, the averaged emission quantum yields for air-stable samples of **1** and **2** at laboratory conditions (ca. 30% RH) reach ca. 0.1–0.2%.

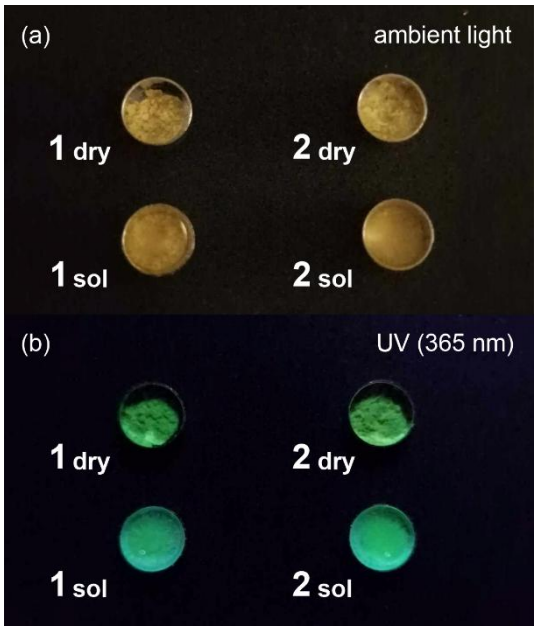

Figure 4. Photos of the powder samples of **1** and **2** under ambient light (a) and upon irradiation by a 20 W 365 nm UV flashlight (b). The ″dry″ subscripts indicate the respective air-stable dry samples (at ca. 30% RH) while the ″sol″ (i.e., solution) subscripts indicate samples covered by a small amount of water.

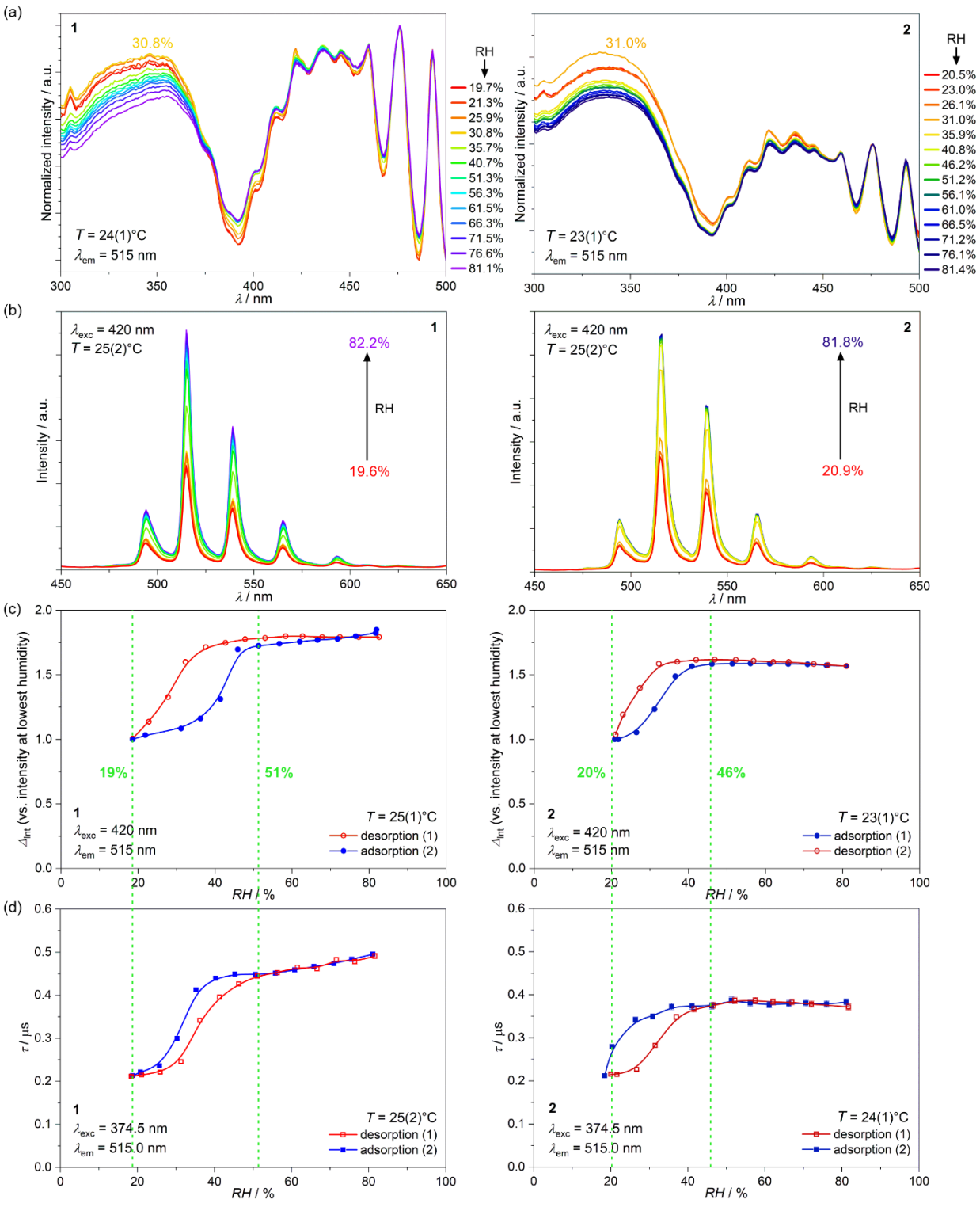

Figure 5. Humidity-variable photoluminescence properties of **1** (left panel) and **2** (right panel), including (a) excitation spectra collected in the water adsorption mode for the 515 nm emission and normalized to the λ_{exc} = 476 nm band (a), emission spectra collected in the water adsorption mode under λ_{exc} = 420 nm (b), humidity variation of the intensity of the λ_{em} = 515 nm emission band in the full cycle of water desorption and adsorption, calculated as the change of the emission intensity versus the intensity at the lowest humidity (i.e., lowest RH value) (c),

humidity variation of the emission lifetime, τ, collected in the full cycle of water desorption and adsorption using λ_{exc} = 374.5 nm laser excitation for λ_{em} = 515 nm (d).

In contrast to the sensitivity of **1** and **2** towards humidity, and the presence of the SC-SC transformation upon the solvent removal, the overall variation of the emission profile is rather subtle, which should be related to coordination skeleton stiffness, stabilizing the geometry of the first coordination sphere for the U(VI) centers, as well as due to the lack of strong supramolecular interactions between solvent molecules and oxido ligands of the uranyl(2+) units. Despite this, upon changing the RH, significant changes within the emission intensity can be observed; therefore, we decided to measure *in situ* humidity-variable emission and excitation spectra, as well as the emission lifetime dependency (**Figure** 5 and S15–S22, **Table** S7). For both presented metallophilic frameworks, upon increasing the RH, the overall emission intensity increased in the ca. 20–82% range, which can be followed using the emission spectra under 420 nm light excitation. However, upon analyzing humidity-variable excitation patterns, not only the overall excitation efficiency change is noticed upon the increase of humidity. Normalization of such a set of spectra to an excitation band centered at 476 nm, which is attributed to the direct excitation pathway of the UO_2^{2+} moieties, indicates a non-monotonous variation of the deep-UV excitation pathway. For both **1** and **2**, the highest intensity of high-energy broad excitation is located at the level of ca. 30% RH, and then drops down, with respect to the direct excitation, upon increasing the humidity. Such observation suggests the involvement of $[M^{II}(CN)_4]^{2-}$ moieties and the related metallophilic interactions in the energy transfer to U(VI) centers. This maximum of the energy transfer efficiency roughly correlates with the change within the adsorption course. This suggests that the adsorption of the third water molecule increases the energy of MMLCT states related to the metallophilic interactions, while the adsorption of the fourth one decreases their energy and/or introduces partial energy quenching through the formation of H-bonding interactions with terminal cyanido ligands of the $[M^{II}(CN)_4]^{2-}$ moieties. However, this subtle effect does not affect the overall increase of the emission upon increasing the RH regardless of the excitation wavelength.

While the adsorption of water vapors usually leads to a decrease of the emission intensity due to the activation of numerous O–H vibrations,[66] quenching radiative relaxation pathways, the inverted effect may be observed, when the presence of additional non-coordinated molecules of crystallization stabilize the H-bonding network.[67] In the case of **1** and **2**, each f-block metal site is bonded to one coordinated aqua ligand, which cannot be removed either upon variation of humidity or via thermal treatment without the loss of crystallinity (see **Figure**

S4). However, the aqua ligand is strongly involved in the formation of O–H…N contacts with terminal cyanido ligands of the $[M^{II}(CN)_4]^{2-}$ units, stabilizing the supramolecular framework; thus should not be considered as the source of luminescence variation. Therefore again, we should consider MMLCT states of the metallophilic interactions' origin as a plausible source of the absolute luminescence variation. Within this scenario, the presence of MMLCT states partially quenches the emission from the uranyl(2+) CT states; thus, upon water uptake, the expansion of the network reduces the overlap between the $[M^{II}(CN)_4]^{2-}$ units. As a result, the energy back-transfer from the excited electronic states of CT origin remains reduced at higher RH. Such an explanation of the humidity-variable emission characteristics is supported by the literature, where for the reported uranyl-based CMC-based systems, the presence of metallophilic interactions was found to quench the emission of the CT origin.[55c] This interpretation also stays in line with the lack of the emission band shift even after removing all the non-coordinated solvent molecules for **1deh** and **2deh** phases. This feature prompted us to follow the humidity variation for absorption and desorption cycles using the 420 nm excitation and collecting the signal at 515 nm (**Figure** 5, S18, and S19). At the lowest reachable RH (19% for **1** and 20% for **2**) the emission signal stays at its minimum for both **1** and **2**. Then, upon changing the humidity, an abrupt increase is observed in the 30-40% RH range. Above 40% RH, further adsorption differentiates **1** from **2**. For **1**, the increase in humidity results in a subtle increase of the emission intensity, while in **2** the observed signal remains stable within the error. This may be correlated to the size of the unit cell, which is generally smaller for **1**, thus the impact of water inclusion upon the expansion of the network should be more significant. At high humidity, the negative impact of the additional O–H should limit the increase of the signal resulting from quenching the MMLCT states. Therefore, within the first steps of desorption curves, for both **1** and **2**, a subtle increase in the signal can be noticed. An abrupt drop of the emission for both materials is observed at the decreased humidity in comparison to the adsorption curves, which indicates the presence of a luminescence memory effect.

A piece of additional information regarding the humidity-dependent emission for **1** and **2** is given by the RH-variable emission lifetime measurements (**Figure** 5 and S20–S22, **Table** S7). Although for both materials, the emission lifetimes at lower humidity values reach smaller values to higher humidity, the trends within the luminescence memory effect are opposite. At the lowest humidity, the extracted lifetimes are at the level of 212(3) ns and 213(2) ns for **1** and **2**, respectively, which is in the short range concerning luminescent uranyl(2+) complexes. Upon water adsorption, the lifetime increases ca. two times after an abrupt step at around 30% of RH. At high humidity, smaller lifetime values of ca. 0.38 μs are found for **2**, suggesting a stronger

influence of metallophilic interactions, which is typical when comparing $[Pt^{II}(CN)_4]^{2-}$– and $[Pd^{II}(CN)_4]^{2-}$-based systems.[68] As for the emission intensity, **1** shows the continuous increase of the lifetime upon water adsorption, reaching its value of 495(5) ns at ca. 80% of RH. Interestingly, upon water desorption, the lifetime behavior follows that of the adsorption, thus only its decrease is observed for **1**, which confirms, that the emission changes are mainly governed by the energy-transfer processes within the excited states of UO_2^{2+} moieties. The opposite trends within the hysteretic behavior of the luminescence memory effect may suggest that structural changes related to the water adsorption occur separately to the reorganization of the H-bonding frameworks between the non-coordinated water molecules; however, the detailed structural analysis was found inefficient in determining the exact positions of H atoms for the non-coordinated solvent, suggesting its partial disorder or mobility within the pores of **1** and **2** frameworks.

To check the stability of the materials within several cycles of water adsorption and desorption, the sets of cycles using the DVS apparatus were performed for both materials (**Figure** 6). Upon variation of relative humidity between 0 and 80% of RH, the observed mass changes reach the same levels within the experimental error at least for four executive cycles. As both materials reveal humidity-dependent emission characteristics, we also studied the related changes in the emission intensity within four cycles of desorption and sorption (**Figure** 6). As a result, almost perfect repeatability of the emission intensity was obtained for both materials, despite small variations of the boundary RH values between the cycles present due to the experimental conditions. Concerning the above, both materials could be considered as unique luminescent humidity sensors, where the emission signal increases its intensity in a highly repeatable manner upon exposition to water vapors.

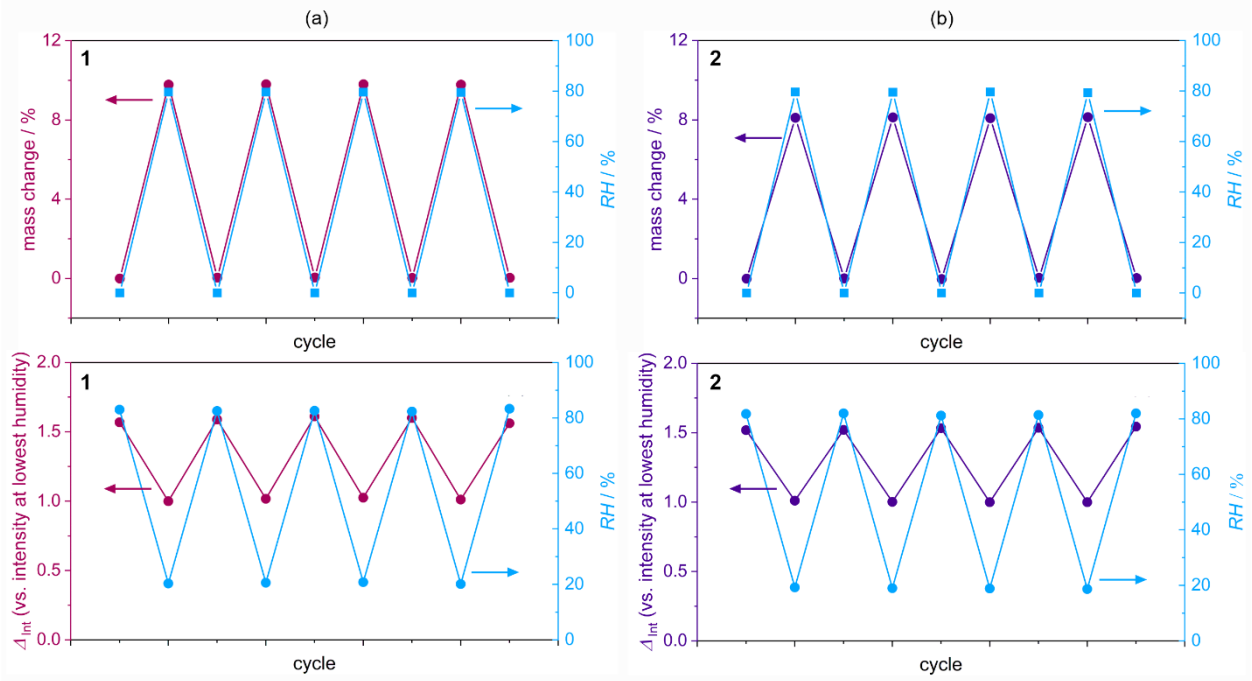

Figure 6. Representative curves of humidity-induced changes in the sample mass (top part) and the changes in the intensity of the λ_{em} = 515 nm emission band (excitation by the 420 nm light), calculated as the change of the emission intensity versus the intensity at the lowest humidity (i.e., lowest RH value, bottom part) for materials **1** (a) and **2** (b) upon the subsequent cycles of desorption–adsorption of water vapors related to the decrease–increase cycles of relative humidity (RH) changes (shown on the right scale of each graph). The related measurements were conducted at 25(1)°C and 26(1)°C for **1** and **2**, respectively.

3. Conclusion

In this work, we presented two novel porous metallophilic frameworks based on metal-organic chains that involve uranium(VI) centers bridged by organic 2,4'-bipyridine-N,N'-dioxide linkers as well as anionic inorganic tetracyanidometallate(II), $[M^{II}(CN)_4]^{2-}$ (M^{II} = Pd, Pt) metalloligands. The presence of the latter results in the formation of the 3-D supramolecular network of topological resemblance to well-known MOF-74, owing to metallophilic interactions between the d-block metal centers serving a non-innocent structural porosity-making role. The obtained porous metallophilic frameworks of the formula of $\{[U^{VI}O_2(2,4'\text{-bpdo})(H_2O)][M^{II}(CN)_4]\}\cdot nH_2O$ (M = Pd, Pt) accommodate within the structural channel-shaped pores additional water molecules, which can be conveniently removed within a reversible single-crystal-to-single-crystal phase transformation. As a result, both materials reveal water sorption properties, here studied precisely using both gravimetric and volumetric methods. Upon UV-vis light irradiation, the presence of uranyl-centered photoluminescence was detected

with a typical charge-transfer emission mechanism. Thanks to the conjunction of water sorption properties related to a porous character and photoluminescence features, the emission signal for both materials depends on the relative humidity of the environment. This humidity variation of luminescence characteristics was followed by the absolute emission intensity changes and by the emission lifetime variation. The obtained results indicate a large increase in the emission intensity and lifetime, ca. twice the original values upon the RH change from 20% to 80% of RH. This was rationalized by the humidity-induced weakening of the metallophilic interactions upon network expansion, removal of MMLCT states, and quenching of the related energy back-transfer processes, increasing the efficiency of the radiative CT electronic transitions centered on uranyl(2+) cations. Thus, the non-trivial mechanism governs the humidity-sensing ability of the obtained frameworks, for which, we demonstrate the pioneering pathway for making the uranyl complexes useful in the construction of a luminescent humidity sensor. The observed changes within luminescence, as well as the sample stability, which were proven within adsorption-desorption cycles, suggest the possible use of the obtained systems as humidity sensors. It also opens the broader perspective for further exploration of emissive uranyl and other actinidyl cations in optical sensing of chemicals when they are embedded in porous materials, especially those taking advantage of coordination and supramolecular approaches, such as the usage of metallophilic interactions between d^8 metal complexes.

Supporting Information

Supporting Information is available from the Wiley Online Library or from the author.
[CCDC 2327761–2327766 contains the supplementary crystallographic data for this paper. These data can be obtained free of charge from The Cambridge Crystallographic Data Centre via www.ccdc.cam.ac.uk/data_request/cif.]

Acknowledgments

This research was financed by the National Science Center of Poland within the OPUS-21 project (grant no. 2021/41/B/ST5/02544), while for the synthetic part of the work, the PRELUDIUM-19 project of the National Science Center of Poland (grant no. 2020/37/N/ST5/02643) is acknowledged. For the measurements performed by Japanese collaborators, the JST FOREST Program (JPMJFR213Q), JSPS Grant-in-Aid for Scientific Research (B) (22H02046), Grant-in-Aid for Scientific Research (A) (20H00369), Grant-in-Aid for Early-Career Scientists (24K17691), and Tsukuba Basic Research Support Program (Type S) are acknowledged.

Received: ((will be filled in by the editorial staff))
Revised: ((will be filled in by the editorial staff))
Published online: ((will be filled in by the editorial staff))

References

[1] ((Journal articles)) a) A. B. Author 1, C. D. Author 2, *Adv. Mater.* **2020**, *18*, 2001086; b) A. Author 1, B. Author 2, *Adv. Funct. Mater.* **2019**, *16*, 1900965.

[1] a) C. Wegeberg, O. S. Wenger, *JACS Au* **2021**, *1*, 1860–1876; b) R. Gao, M. S. Kodaimati, D. Yan, *Chem. Soc. Rev.* **2021**, *50*, 5564–5589; c) Y. Cui, Y. Yue, G. Qian, B. Chen, *Chem. Rev.* **2012**, *112*, 1126–1162; d) M. D. Allendorf, C. A. Bauer, R. K. Bhakta, R. J. T. Houk, *Chem. Soc. Rev.* **2009**, *38*, 1330–1352.

[2] L. D. Carlos, R. A. S. Ferreira, V. d. Z. Bermudez, S. J. L. Ribeiro, *Adv. Mater.* **2009**, *21*, 509–534.

[3] J. Sun, J. Wang, M. Chen, X. Pu, G. Wang, L. Li, G. Chen, Y. Cai, X. Gu, B. Z. Tang, *Chem. Mater.* **2019**, *31*, 5683–5690.

[4] a) C. D. S. Brites, S. Balabhadra, L. D. Carlos, *Adv. Optical Mater.* **2019**, *7*, 1801239; b) M. Runowski, D. Marcinkowski, K. Soler-Carracedo, A. Gorczyński, E. Ewert, P. Woźny, I. R. Martín, *ACS Appl. Mater. Interfaces* **2023**, *15*, 3244–3252; c) C. D. S. Brites, P. P. Lima, N. J. O. Silva, A. Millán, V. S. Amaral, F. Palacio, L. D. Carlos, *Adv. Mater.* **2010**, *22*, 4499–4504.

[5] a) M. Annadhasan, U. Venkataramudu, N. V. Mitetelo, E. A. Mamonov, C. Sahoo, S. R. G. Naraharisetty, T. V. Murzina, R. Chandrasekar, *ACS Appl. Energy Mater.* **2019**, *2*, 428–435; b) X. Huang, S. Han, W. Huang, X. Liu, *Chem. Soc. Rev.* **2013**, *42*, 173–201**.**

[6] J.-C. G. Bünzli, *Chem. Rev.* **2010**, *110*, 2729–2755.

[7] a) R.-B. Lin, S.-Y. Liu, J.-W. Ye, X.-Y. Li, J.-P. Zhang, *Adv. Sci.* **2016**, *3*, 1500424; b) S. Pramanik, C. Zheng, X. Zhang, T. J. Emge, J. Li, *J. Am. Chem. Soc.* **2011**, *133*, 4153–4155; c) S. E. Bodman, S. J. Butler, *Chem. Sci.* **2021**, *12*, 2716–2734; d) M. Li, Q. Shi, N. Song, Y. Xiao, L. Wang, Z. Chen, T. D. James, *Chem. Soc. Rev.* **2023**, *52*, 5827–5860.

[8] a) Y. Chi, P.-T. Chou, *Chem. Soc. Rev.* **2010**, *39*, 638–655; b) J.-Q. Liu, Z.-D. Luo, Y. Pan, A. K. Singh, M. Trivedi, A. Kumar, *Coord. Chem. Rev.* **2020**, *406*, 213145.

[9] a) Y. Xin, J. Wang, M. Zychowicz, J. J. Zakrzewski, K. Nakabayashi, B. Sieklucka, S. Chorazy, S. Ohkoshi, *J. Am. Chem. Soc.* **2019**, *141*, 18211–18220; b) J. J. Zakrzewski, M. Liberka, J. Wang, S. Chorazy, S. Ohkoshi, *Chem. Rev.* **2024**, *124*, 5930–6050; c) W. Zhang, S. Jiao, M. Zhao, C. Xu, Z. Yang, D. Li, Z. Tang, Y. Lu, H.-L. Cai, X.-S. Wu, *J. Phys. Chem. C*

2023, *127*, 17261–17268; d) Y. Zhang, W. Jie, P. Chen, W. Liu, J. Hao, *Adv. Mater.* **2018**, *30*, 1707007; e) M. Liberka, M. Zychowicz, J. Hooper, K. Nakabayashi, S. Ohkoshi, S. Chorazy, *Angew. Chem. Int. Ed.* **2023**, *62*, e202308284; f) B. Huitorel, Q. Benito, A. Fargues, A. Garcia, T. Gacoin, J.-P. Boillot, S. Perruchas, F. Camerel, *Chem. Mater.* **2016**, *28*, 8190–8200.

[10] a) M. Hasegawa, H. Ohmagari, H. Tanaka, K. Machida, *J. Photochem. Photobiol. C* **2022**, *50*, 100484; b) J.-X. Wang, J. Yin, O. Shekhah, O. M. Bakr, M. Eddaoudi, O. F. Mohammed, *ACS Appl. Mater. Interfaces* **2022**, *14*, 9970–9986; c) D. Zhao, K. Yu, X. Han, Y. He, B. Chen, *Chem. Commun.* **2022**, *58*, 747–770; d) M. Gutiérrez, Y. Zhang, J.-C. Tan, *Chem. Rev.* **2022**, *122*, 10438–10483.

[11] a) G. E. Decker, G. R. Lorzing, M. M. Deegan, E. D. Bloch, *J. Mater. Chem. A* **2020**, *8*, 4217–4229; b) G. Zhang, B. Li, Y. Zhou, X. Chen, B. Li, Z.-Y. Lu, L. Wu, *Nat. Commun*. **2020**, *11*, 425; c) S. Chang, Y. Chen, H. An, Q. Zhu, H. Luo, Y. Huang, *Green Chem*. **2021**, *23*, 8591–8603; d) C. Zhang, Z. Wang, W.-D. Si, H. Chu, L. Zhou, T. Li, X.-Q. Huang, Z.-Y. Gao, M.; Azam, C.-H. Tung, P. Cui, D. Sun, *Nat. Commun*. **2023**, *14*, 6413; e) X. Tang, J. Pang, J. Dong, Y. Liu, X.-H. Bu, Y. Cui, *Angew. Chem. Int. Ed*. **2024**, *63*, e202406956.

[12] a) S. L. James, *Chem. Soc. Rev.* **2003**, *32*, 276–288; b) S. Ohkoshi, K. Arai, Y. Sato, K. Hashimoto, *Nature Mater*. **2004**, *3*, 857–861; c) L. E. Kreno, K. Leong, O. K. Farha, M. Allendorf, R. P. Van Duyne, J. T. Hupp, *Chem. Rev.* **2012**, *112*, 1105–1125; d) M. D. Allendorf, R. Dong, X. Feng, S. Kaskel, D. Matoga, V. Stavila, *Chem. Rev.* **2020**, *120*, 8581–8640; e) S. E. Skrabalak, R. Vaidhyanathan, *Chem. Mater.* **2023**, *35*, 5713–5722.

[13] A. C. Forse, K. A. Colwell, M. I. Gonzalez, S. Benders, R. M. Torres-Gavosto, B. Blümich, J. A. Reimer, J. R. Long, *Chem. Mater.* **2020**, *32*, 3570–3576.

[14] V. Pascanu, G. G. Miera, A. K. Inge, B. Martín-Matute, *J. Am. Chem. Soc.* **2019**, *141*, 7223–7234.

[15] G. E. Gomez, R. Marin, A. N. Carneiro Neto, A. M. P. Botas, J. Ovens, A. A. Kitos, M. C. Bernini, L. D. Carlos, G. J. A. A. Soler-Illia, M. Murugesu, *Chem. Mater.* **2020**, *32*, 7458–7468.

[16] L. Xu, X. Xiao, H. Tu, F. Zhu, J. Wang, H. Liu, W. Huang, W. Deng, H. Hou, T. Liu, X. Ji, K. Amine, G. Zou, *Adv. Mater.* **2023**, *35*, 2303193.

[17] M.-X. Wu, Y.-W. Yang, *Adv. Mater.* **2017**, *29*, 1606134.

[18] S.-M. Wang, X.-T. Mu, H.-R. Liu, S.-T. Zheng, Q.-Y. Yang, *Angew. Chem. Int. Ed.* **2022**, *61*, e202207066.

[19] a) M. P. Suh, H. J. Park, T. K. Prasad, D.-W. Lim, *Chem. Rev.* **2012**, *112*, 782–835; b) N. L. Rosi, J. Eckert, M. Eddaoudi, D. T. Vodak, J. Kim, M. O'Keeffe, O. M. Yaghi, *Science* **2003**, *300*, 1127–1129.

[20] a) W. Li, X. Xia, M. Cao, S. Li, *J. Mater. Chem. A* **2019**, *7*, 7470–7479; b) S. Chen, B. E. G. Lucier, P. D. Boyle, Y. Huang, *Chem. Mater.* **2016**, *28*, 5829–5846.

[21] a) X. Kang, Z. Jiao, X. Shi, Y. Tian, Z. Liu, *J. Mater. Chem. C* **2022**, *10*, 16078–16087; b) S. Bej, S. Mandal, A. Mondal, T. K. Pal, P. Banerjee, *ACS Appl. Mater. Interfaces* **2021**, *13*, 25153–25163.

[22] a) M.-K. Sit, G. S. M. Tong, T.-L. Lam, G. Cheng, F.-F. Hung, K.-M. So, L. Du, K.-O. Choy, K.-H. Low, C.-M. Che, *Adv. Optical Mater.* **2024**, *12*, 2302308; b) J. Ma, J. Schaab, S. Paul, S. R. Forrest, P. I. Djurovich, M. E. Thompson, *J. Am. Chem. Soc.* **2023**, *145*, 20097–20108; c) H. Amouri, *Chem. Rev.* **2023**, *123*, 230–270.

[23] a) J.-C. G. Bünzli, *Chem. Rev.* **2010**, *110*, 2729–2755; b) J.-C. G. Bünzli, C. Piguet, *Chem. Soc. Rev.* **2005**, *34*, 1048–1077; c) K. Binnemans, *Chem. Rev.* **2009**, *109*, 4283–4374; d) S. Sun, Y. Zhao, J. Wang, R. Pei, *J. Mater. Chem. B* **2022**, *10*, 9535–9564; e) J. J. Zakrzewski, M. Liberka, M. Zychowicz, S. Chorazy, *Inorg. Chem. Front.* **2021**, *8*, 452–483.

[24] a) N. B. D. Lima, S. M. C. Gonçalves, S. A. Júnior, A. M. Simas, *Sci. Rep.* **2013**, *3*, 2395; b) Y. Zhang, X. Wang, K. Xu, F. Zhai, J. Shu, Y. Tao, J. Wang, L. Jiang, L. Yang, Y. Wang, J. Liu, Z. Chai, S. Wang, *J. Am. Chem. Soc.* **2023**, *145*, 13161–13168.

[25] Z. Hu, B. J. Deibert, J. Li, *Chem. Soc. Rev.* **2014**, *43*, 5815–5840.

[26] X. Shen, B. Yan, *J. Mater. Chem. C* **2015**, *3*, 7038–7044.

[27] J.-H. Wang, M. Li, D. Li, *Chem. Sci.* **2013**, *4*, 1793–1801.

[28] N. D. Rudd, H. Wang, E. M. A. Fuentes-Fernandez, S. J. Teat, F. Chen, G. Hall, Y. J. Chabal, J. Li, *ACS Appl. Mater. Interfaces* **2016**, *8*, 30294–30303.

[29] P. Daga, S. Sarkar, P. Majee, D. K. Singha, S. Hui, P. Mahata, S. K. Mondal, *Mater. Adv.* **2021**, *2*, 985–995.

[30] S. S. Nagarkar, B. Joarder, A. K. Chaudhari, S. Mukherjee, S. K. Ghosh, *Angew. Chem. Int. Ed.* **2013**, *52*, 2881–2885.

[31] J. Dong, D. Zhao, Y. Lu, W.-Y. Sun, *J. Mater. Chem. A* **2019**, *7*, 22744–22767.

[32] a) M. Liu, J. Kan, Y. Yao, Y. Zhang, B. Bian, Z. Tao, Q. Zhu, X. Xiao, *Sens. Actuators B: Chem.* **2019**, *283*, 290–297; b) S. Cai, Z. An, W. Huang, *Adv. Funct. Mater.* **2022**, *32*, 2207145; c) M. Kato, M. Yoshida, Y. Sun, A. Kobayashi, *J. Photochem. Photobiol. C: Photochem. Rev.* **2022**, *51*, 100477; d) I. V. Kashnik, B. Yang, S. S. Yarovoi, T. S. Sukhikh, M. Cordier, G. Taupier, K. A. Brylev, P.-A. Vouit, Y. Molard, *Chem. Eur. J.* **2024**, *30*, e202400079.

[33] a) M. B. Andrews, C. L. Cahill, *Chem. Rev.* **2013**, *113*, 1121–1136; b) P. Li, N. A. Vermeulen, C. D. Malliakas, D. A. Gómez-Gualdrón, A. J. Howarth, B. L. Mehdi, A. Dohnalkova, N. D. Browning, M. O'Keeffe, O. K. Farha, *Science* **2017**, *356*, 624–627; c) K.-

X. Wang, J.-S. Chen, *Acc. Chem. Res.* **2011**, *44*, 531–540; d) A. M. Hastings, D. Ray, W. Jeong, L. Gagliardi, O. K. Farha, A. E. Hixon, *J. Am. Chem. Soc.* **2020**, *142*, 9363–9371; e) E. Rheinfrank, M. Pörtner, M. d. C. N. Beyerle, F. Haag, P. S. Deimel, F. Allegretti, K. Seufert, J. V. Barth, M.-L. Bocquet, P. Feulner, W. Auwärter, *J. Am. Chem. Soc.* **2021**, *143*, 14581–14591.

[34] a) J. J. Baldoví, S. Cardona-Serra, J. M. Clemente-Juan, E. Coronado, A. Gaita-Ariño, *Chem. Sci.* **2013**, *4*, 938–946; b) V. Mougel, L. Chatelain, J. Pécaut, R. Caciuffo, E. Colineau, C. Griveau, M. Mazzanti, *Nat. Chem.* **2012**, *4*, 1011–1017.

[35] a) S. L. Hanna, O. K. Farha, *Chem. Sci.* **2023**, *14*, 4219–4229; b) C. R. Martin, G. A. Leith, N. B. Shustova, *Chem. Sci.* **2021**, *12*, 7214–7230; c) E. A. Dolgopolova, A. M. Rice, N. B. Shustova, *Chem. Commun.* **2018**, *54*, 6472–6483; d) K. Lv, S. Fichter, M. Gu, J. März, M. Schmidt, *Coord. Chem. Rev.* **2021**, *446*, 214011.

[36] a) G.-L. Law, C. M. Andolina, J. Xu, V. Luu, P. X. Rutkowski, G. Muller, D. K. Shuh, J. K. Gibson, K. N. Raymond, *J. Am. Chem. Soc.* **2012**, *134*, 15545–15549; b) D. Schnable, N. D. Schley, G. Ung, *J. Am. Chem. Soc.* **2022**, *144*, 10718–10722.

[37] D.-H. Chen, N. Vankova, G. Jha, X. Yu, Y. Wang, L. Lin, F. Kirschhöfer, R. Greifenstein, E. Redel, T. Heine, C. Wöll, *Angew. Chem. Int. Ed.* **2024**, *63*, e202318559.

[38] a) B. E. Cowie, J. M. Purkis, J. Austin, J. B. Love, P. L. Arnold, *Chem. Rev.* **2019**, *119*, 10595–10637; b) J. G. West, T. A. Bedell, E. J. Sorensen, *Angew. Chem. Int. Ed.* **2016**, *55*, 8923–8927; c) X. Zhang, P. Li, M. Krzyaniak, J. Knapp, M. R. Wasielewski, O. K. Farha, *Inorg. Chem.* **2020**, *59*, 16795–16798.

[39] a) A. R. Fox, S. C. Bart, K. Meyer, C. C. Cummins, *Nature* **2008**, *455*, 341–349; b) M. Falcone, L. Barluzzi, J. Andrez, F. F. Tirani, I. Zivkovic, A. Fabrizio, C. Corminboeuf, K. Severin, M. Mazzanti, *Nat. Chem.* **2019**, *11*, 154–160; c) J. D. Rinehart, J. R. Long, *J. Am. Chem. Soc.* **2009**, *131*, 12558–12559; d) D. P. Mills, F. Moro, J. McMaster, J. van Slageren, W. Lewis, A. J. Blake, S. T. Liddle, *Nat. Chem.* **2011**, *3*, 454–460.

[40] P. Li, N. A. Vermeulen, X. Gong, C. D. Malliakas, J. F. Stoddart, J. T. Hupp, O. K. Farha, *Angew. Chem. Int. Ed.* **2016**, *55*, 10358–10362.

[41] a) D. K. Unruh, K. Gojdas, A. Libo, T. Z. Forbes, *J. Am. Chem. Soc.* **2013**, *135*, 7398–7401; b) S. L. Hanna, X. Zhang, K.-i. Otake, R. J. Drout, P. Li, T. Islamoglu, O. K. Farha, *Cryst. Growth Des.* **2019**, *19*, 506–512.

[42] a) J. Xie, Y. Wang, W. Liu, X. Yin, L. Chen, Y. Zou, J. Diwu, Z. Chai, T. E. Albrecht-Schmitt, G. Liu, S. Wang, *Angew. Chem. Int. Ed.* **2017**, *56*, 7500–7504; b) F. Li, L. Mei, K. Hu, S. An, S. Wu, N. Liu, Z. Chai, W.-q. Shi, *Inorg. Chem.* **2019**, *58*, 3271–3282; c) Y. Wang, Z. Liu, Y. Li, Z. Bai, W. Liu, Y. Wang, X. Xu, C. Xiao, D. Sheng, J. Diwu, J. Su, Z. Chai, T.

E. Albrecht-Schmitt, S. Wang, *J. Am. Chem. Soc.* **2015**, *137*, 6144–6148; d) L. Wang, B. Tu, W. Xu, Y. Fu, Y. Zheng, *Inorg. Chem.* **2020**, *59*, 5004–5017; e) S. Yang, J. Hu, J. Zhang, T. He, L. Zhang, H. Chen, *Inorg. Chim. Acta* **2022**, *536*, 120914; f) R. G. Surbella III, K. P. Carter, T. D. Lohrey, D. Reilly, M. Kalaj, B. K. McNamara, J. Schwantes, R. Abergel, *Chem. Eur. J.* **2020**, *26*, 13819–13825; g) L. Wang, W. Xu, W.-Y. Li, M. Xie, Y.-Q. Zheng, *Chem. Asian J.* **2019**, *14*, 4246–4254.

[43] a) P. Thuéry, J. Harrowfield, *Coord. Chem. Rev.* **2024**, *510*, 215821; b) S. Chorazy, J. J. Zakrzewski, M. Reczyński, B. Sieklucka, *Chem. Commun.* **2019**, *55*, 3057–3060; c) M. L. Brown, D. B. Leznoff, *Can. J. Chem.* **2020**, *98*, 365–372; d) B. A. Maynard, R. E. Sykora, J. T. Mague, A. E. V. Gorden, *Chem. Commun.* **2010**, *46*, 4944–4946; e) M. L. Brown, J. S. Ovens, D. B. Leznoff, *Dalton Trans.* **2017**, *46*, 7169–7180; f) P. A. Smith, S. M. Hickam, J. E. S. Szymanowski, P. C. Burns, *Inorg. Chem.* **2018**, *57*, 9504–9514; g) B. A. Maynard, S. Lynn, R. E. Sykora, A. E. V. Gorden, *Inorg. Chem.* **2013**, *52*, 4880–4889.

[44] a) S. Chorazy, J. J. Zakrzewski, M. Magott, T. Korzeniak, B. Nowicka, D. Pinkowicz, R. Podgajny, B. Sieklucka, *Chem. Soc. Rev.* **2020**, *49*, 5945–6001; b) S. Chorazy, K. Nakabayashi, S. Ohkoshi, B. Sieklucka, B. *Chem. Mater.* **2014**, *26*, 4072–4075; c) W.-J. Xu, K. Romanyuk, J. M. G. Martinho, Y. Zeng, X.-W. Zhang, A. Ushakov, V. Shur, W.-X. Zhang, X.-M. Chen, A. Kholkin, J. Rocha, *J. Am. Chem. Soc.* **2020**, *142*, 16990–16998; d) S. G. Duyker, V. K. Peterson, G. J. Kearley, A. J. Studer, C. J. Kepert, *Nat. Chem.* **2016**, *8*, 270–275.

[45] a) D. Pinkowicz, M. Rams, M. Mišek, K. K. Kamenev, H. Tomkowiak, A. Katrusiak, B. Sieklucka, *J. Am. Chem. Soc.* **2015**, *137*, 8795–8802; b) J. Wang, J. J. Zakrzewski, M. Heczko, M. Zychowicz, K. Nakagawa, K. Nakabayashi, B. Sieklucka, S. Chorazy, S. Ohkoshi, *J. Am. Chem. Soc.* **2020**, *142*, 3970–3979; c) S. Ohkoshi, S. Takano, K. Imoto, M. Yoshikiyo, A. Namai, H. Tokoro, *Nat. Photonics* **2014**, *8*, 65–71.

[46] S. Chorazy, M. Wyczesany, B. Sieklucka, *Molecules* **2017**, *22*, 1902.

[47] S. Chorazy, T. Charytanowicz, D. Pinkowicz, J. Wang, K. Nakabayashi, S. Klimke, F. Renz, S. Ohkoshi, B. Sieklucka, *Angew. Chem. Int. Ed.* **2020**, *59*, 15741–15749.

[48] a) M. Reczyński, D. Pinkowicz, K. Nakabayashi, C. Näther, J. Stanek, M. Kozieł, J. Kalinowska-Tłuścik, B. Sieklucka, S. Ohkoshi, B. Nowicka, *Angew. Chem. Int. Ed.* **2021**, *60*, 2330–2338; b) Q. Li, X. Sha, S. Li, K. Wang, Z. Quan, Y. Meng, B. Zou, *J. Phys. Chem. Lett.* **2017**, *8*, 2745–2750; c) H. Yersin, D. Trümbach, J. Strasser, H. H. Patterson, Z. Assefa, *Inorg. Chem.* **1998**, *37*, 3209–3216.

[49] a) S. Ohkoshi, K. Imoto, Y. Tsunobuchi, S. Takano, H. Tokoro, *Nat. Chem.* **2011**, *3*, 564–569; b) C. Mathonière, R. Podgajny, P. Guionneau, C. Labrugere, B. Sieklucka, *Chem. Mater.* **2005**, *17*, 442–449.

[50] M. Ohba, K. Yoneda, G. Agustí, M. C. Muñoz, A. B. Gaspar, J. A. Real, M. Yamasaki, H. Ando, Y. Nakao, S. Sakaki, S. Kitagawa, *Angew. Chem. Int. Ed.* **2009**, *48*, 4767–4771.

[51] a) G. Agustí, R. Ohtani, K. Yoneda, A. B. Gaspar, M. Ohba, J. Sánchez-Royo, M. C. Muñoz, S. Kitagawa, *Angew. Chem. Int. Ed.* **2009**, *48*, 8944–8947; b) G.-Z. Huang, Y.-S. Xia, F. Yang, W.-J. Long, J.-J. Liu, J.-P. Liao, M. Zhang, J. Liu, Y.-Q. Lan, *J. Am. Chem. Soc.* **2023**, *145*, 26863–26870.

[52] a) D. Pinkowicz, R. Podgajny, B. Gaweł, W. Nitek, W. Łasocha, M. Oszajca, M. Czapla, M. Makarewicz, M. Bałanda, B. Sieklucka, *Angew. Chem. Int. Ed.* **2011**, *50*, 3973–3977; b) D. Pinkowicz, R. Podgajny, W. Nitek, M. Rams, A. M. Majcher, T. Niuda, S. Ohkoshi, B. Sieklucka, *Chem. Mater.* **2011**, *23*, 21–31; c) Q. Gao, J. Chen, Q. Sun, D. Chang, Q. Huang, H. Wu, A. Sanson, R. Milazzo, H. Zhu, Q. Li, Z. Liu, J. Deng, X. Xing, *Angew. Chem. Int. Ed.* **2017**, *56*, 9023–9028; d) M. Reczyński, S. Chorazy, B. Nowicka, B. Sieklucka, S. Ohkoshi, *Inorg. Chem.* **2017**, *56*, 179–185; e) M. Reczyński, B. Nowicka, C. Näther, M. Kozieł, K. Nakabayashi, S. Ohkoshi, B. Sieklucka, *Inorg. Chem.* **2018**, *57*, 13415–13422; f) J. Wang, J. J. Zakrzewski, M. Zychowicz, Y. Xin, H. Tokoro, S. Chorazy, S. Ohkoshi, *Angew. Chem. Int. Ed.* **2023**, *62*, e202306372; g) M. Magott, M. Reczyński, B. Gaweł, B. Sieklucka, D. Pinkowicz, *J. Am. Chem. Soc.* **2018**, *140*, 15876–15882.

[53] S. Chorazy, J. J. Zakrzewski, M. Reczyński, K. Nakabayashi, S. Ohkoshi, B. Sieklucka, *J. Mater. Chem. C* **2019**, *7*, 4164–4172.

[54] J. J. Zakrzewski, M. Heczko, R. Jankowski, S. Chorazy, *Molecules* **2021**, *26*, 1102.

[55] a) M. L. Brown, D. B. Leznoff, *Can. J. Chem.* **2020**, *98*, 365–372; b) B. A. Maynard, R. E. Sykora, J. T. Mague, A. E. V. Gorden, *Chem. Commun.* **2010**, *46*, 4944–4946; c) M. L. Brown, J. S. Ovens, D. B. Leznoff, *Dalton Trans.* **2017**, *46*, 7169–7180.

[56] G. M. Sequeira, W. Y. Tan, E. G. Moore, *Dalton Trans.* **2015**, *44*, 13378–13383..

[57] a) G. M. Sheldrick, *Acta Cryst., Sect. A: Found. Adv.* **2015**, *A71*, 3–8; b) G. M. Sheldrick, *Acta Cryst., Sect. C: Struct. Chem.* **2015**, *C71*, 3–8; c) L. J. Farrugia, *J. Appl. Cryst.* **1999**, *32*, 837–838.

[58] a) D. Casanova, J. Cirera, M. Llunell, P. Alemany, D. Avnir, S. Alvarez, *J. Am. Chem. Soc.* **2004**, *126*, 1755–1763; b) M. Llunell, D. Casanova, J. Cirera, J. Bofill, P. Alemany, S. Alvarez, M. Pinsky, D. Avnir, SHAPE v. 2.1. Program for the Calculation of Continuous Shape

Measures of Polygonal and Polyhedral Molecular Fragments, University of Barcelona, Barcelona, Spain, **2013**.

[59] a) K. Tan, S. Ullah, H. Pandey, E. M. Cedeño-Morales, H. Wang, K. Wang, H.-C. Zhou, J. Li, T. Thonhauser, *Chem. Mater.* **2022**, *34*, 7906–7915; b) H. Kim, C. S. Hong, *CrystEngComm* **2021**, *23*, 1377–1387; c) M. Magott, D. Pinkowicz, *Chem. Commun.* **2021**, *57*, 9926–9929.

[60] C. F. Macrae, P. R. Edgington, P. McCabe, E. Pidcock, G. P. Shields, R. Taylor, M. Towler, J. van de Streek, *J. Appl. Cryst.* **2006**, *39*, 453–457.

[61] N. J. Robinson, P. A. Smith, S. Grant, K. Whitehead, C. Crawford, Z. Assefa, R. E. Sykora, *Inorg. Chim. Acta* **2013**, *394*, 459–465.

[62] W. R. Mason III, H. B. Gray, *J. Am. Chem. Soc.* **1968**, *90*, 5721–5729.

[63] J. Rouquerol, P. Llewellyn, F. Rouquerol, *Stud. Surf. Sci. Catal.* **2007**, *160*, 49–56.

[64] a) S. Sircar, R. Mohr, C. Ristic, M. B. Rao, *J. Phys. Chem. B* **1999**, *103*, 6539–6546; b) A. Nuhnen, C. Janiak, *Dalton Trans.* **2020**, *49*, 10295–10307.

[65] R. G. Surbella III, L. C. Ducati, J. Autschbach, N. P. Deifel, C. L. Cahill, *Inorg. Chem.* **2018**, *57*, 2455–2471.

[66] K. Wu, T. Fei, T. Zhang, *Nanomaterials* **2022**, *12*, 4208.

[67] a) S. Mohapatra, B. Rajeswaran, A. Chakraborty, A. Sundaresan, T. K. Maji, *Chem. Mater.* **2013**, *25*, 1673–1679; b) D. Wang, Q. Tan, J. Liu, Z. Liu, *Dalton Trans.* **2016**, *45*, 18450–18454; c) Y. Yu, J.-P. Ma, Y.-B. Dong, *CrystEngComm* **2012**, *14*, 7157–7160.

[68] J. J. Zakrzewski, B. Sieklucka, S. Chorazy, *Inorg. Chem.* **2020**, *59*, 1393–1404.

The table of contents entry:

Porous Metallophilic Frameworks Incorporating Metal-Organic Chains as Humidity Sensors Exploring Uranyl Photoluminescence

J. J. Zakrzewski,* D. Jędrzejowski, J. Wang, H. Tokoro, S. Ohkoshi, D. Matoga, S. Chorazy*

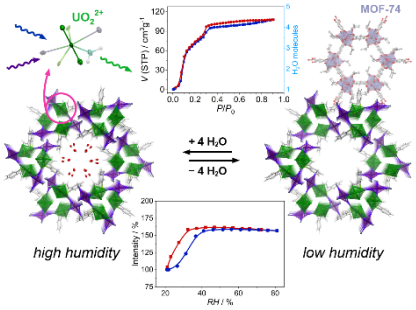

Uranyl cations demonstrating distinct charge-transfer-type visible photoluminescence are incorporated into metal-organic chains with 2,4'-bipyridine-N,N'-dioxide that are further arranged into a unique porous supramolecular framework, resembling the MOF-74 structure, stabilized by metallophilic interactions between attached tetracyanidometallates. As a result, the uranyl luminescence is forced to be applicable for efficient optical sensing of humidity.